Electrostatic Lenses for Laboratory Spacecraft Wake Generation

Kaylee Champion and Hanspeter Schaub

***Abstract*—Cislunar spacecraft may be mesothermal with respect to ambient plasma, generating spacecraft ion wakes. It is unknown that how these wake formations impact technologies, such as touchless potential sensing and the electrostatic tractor. Therefore, wakes are generated in the Electrostatic Charging Laboratory for Interactions between Plasma and Spacecraft (ECLIPS) vacuum chamber at the University of Colorado at Boulder to determine how to account for and take advantage of the wake formations. The natural ion beam generated in the chamber is too small to place a several centimeter-sized objects in the wake and expands radially outward. To correct this, electrostatic lens configurations are designed to expand and refocus the ion beam. Optimization algorithms are used to determine the ideal electrostatic lens configuration, and the design, installation, and characterization of these lenses are presented. The experimental and numerical simulations show good agreement, enabling the installation of simple electrostatic lenses for ion beam manipulation in vacuum systems. Representative cislunar spacecraft wakes are then successfully generated and measured in the ECLIPS vacuum chamber.**

***Index Terms*—Electrostatic lenses, particle beam optics, plasma measurements.**

I. Introduction

NOVEL active potential sensing methods have been investigated for application in the geosynchronous region (GEO). The active potential sensing involves a servicing spacecraft directing an electron beam at a target so that secondary electrons [1], [2], [3], [4] and X-rays [5], [6], [7], [8] are emitted from the surface. The use of a vacuum ultraviolet laser has also been investigated as a method to excite photoemissions from a target [9]. The energy of the incoming signals is then measured, and the servicer utilizes the measurements to infer the potential of the target with respect to its own potential. This potential measurement can be used to avoid electrostatic discharges during docking procedures, account for perturbing electrostatic torques during proximity operations, and provide a step toward electrostatic actuation. Electrostatic actuation can be used to detumble or reorbit uncooperative targets, dock to incoming bodies, and conduct touchless in situ servicing [10], [11], [12], [13], [14], [15], [16], [17], [18]. As more missions are designated for cislunar space, this technology may be expanded there as well. However, the complexity of the cislunar environment presents novel challenges for touchless potential sensing.

When a spacecraft travels through plasma, the ambient electrons and ions are deflected. In hot plasma environments, the ions and electrons are capable of catching back up to the spacecraft and continuing to impact on all sides. In less energetic plasma environments, the thermal velocity of the ions v_i is less than the velocity of the spacecraft v_{sc}, meaning that the spacecraft is mesothermal with respect to the plasma ($v_i < v_{sc} < v_e$). It should be noted that this is the velocity of the spacecraft with respect to the plasma or the velocity of the spacecraft minus the bulk flow of the plasma v_{bulk}. In these conditions, it may take several spacecraft lengths for the ions to catch back up, leaving a complex ion-void region on the antivelocity side of the spacecraft and a high-density ion region on the ram side [19]. This results in varying plasma and potential field conditions around the spacecraft that can alter electron beam and electron emission trajectories. Spacecraft wakes are more rarified in GEO and can be neglected, so their impact on touchless potential sensing has not been investigated.

Numerical programs, such as Nascap-2k [20] and SPIS [21], can be utilized to investigate spacecraft-plasma interactions and electron emissions. Simulations are excellent resources and can provide insight into wake formations about spacecraft with large potentials [22], [23], [24], the impact of wakes on surface charging [25], [26], [27], [28], and the effect wakes have on scientific instruments [29], [30]. However, these programs include assumptions about the space environment and interactions that may not capture the actual conditions. For example, the electron emissions or electron beam may follow different trajectories in different regions of the wake, or small changes in the potential field due to the wake and electron beam may not be captured in simulations. Therefore, it is desirable to complement numerical simulations with experimental results to validate the modeled behavior acceptably represents realistic scenarios. This study focuses on enabling spacecraft wake generation in the Electrostatic Charging Laboratory for Interactions between Plasma and Spacecraft (ECLIPS) vacuum chamber located at the Autonomous Vehicles Systems (AVS) Laboratory, University of Colorado at Boulder.

Spacecraft wake experiments have been extensively conducted to broaden our understanding of the wake phenomena

Received 4 December 2024; revised 16 January 2025; accepted 18 February 2025. Date of publication 21 March 2025; date of current version 14 April 2025. This work was supported by the National Aeronautics and Space Administration (NASA) Space Technology Graduate Research Opportunity under Grant 80NSSC22K1175. The review of this article was arranged by Senior Editor C. A. Ekdahl. *(Corresponding author: Kaylee Champion.)*

The authors are with the Ann and H.J. Smead Department of Aerospace Engineering Sciences and Colorado Center for Astrodynamics Research, University of Colorado at Boulder, Boulder, CO 80309 USA (e-mail: kaylee.champion@colorado.edu).

Color versions of one or more figures in this article are available at https://doi.org/10.1109/TPS.2025.3547749.

Digital Object Identifier 10.1109/TPS.2025.3547749

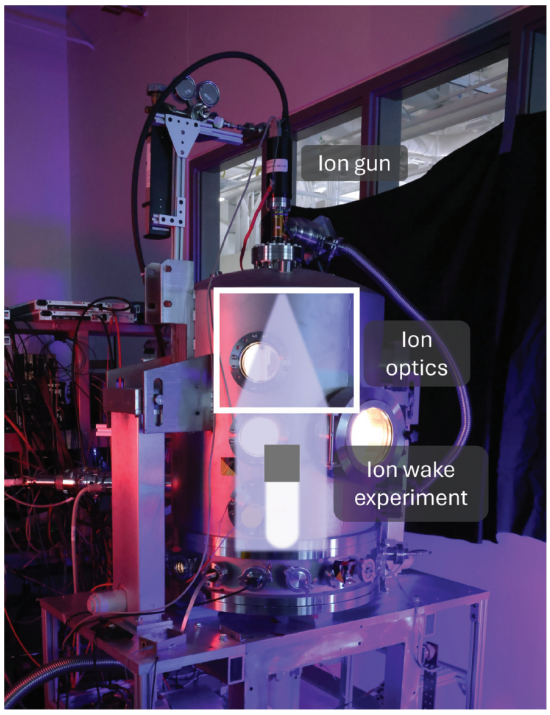

Fig. 1. Proposed ion wake experimental implementation in the ECLIPS vacuum chamber.

and its impact on spacecraft missions. Several laboratory experiments have helped determine properties of a spacecraft wake [31], [32], [33], [34], [35], characterize how wake formation may alter space plasma measurements [36], [37], and even investigate how cislunar wakes impact lunar regolith charging [38]. These experiments involve an ion or plasma source, an object to obstruct the flow of plasma, and sensors, such as Langmuir probes (LPs) and Faraday cups to determine the properties of the plasma. It would be straightforward to implement a similar setup in the ECLIPS vacuum chamber. However, the 1402 Ion Gun from Non Sequitur Technologies installed in the ECLIPS chamber emits a narrow ion beam that may not be sufficient to fully surround an object and generate an ion wake. A cube with a minimal width of 5 cm is required for touchless potential sensing experiments based on previous experiments. This allows the entire electron gun to impact the face of the cube. Furthermore, there should be at least 1 cm of ions surrounding the cube to ensure measurements can be made of the fast-flowing ions and wake formation. The diagonal of a 5 cm cube is approximately 7.1 cm, so the beam should have a radius of at least 4.55 cm. In addition, the beam expands radially outwards throughout the length of the chamber, which does not represent the parallel flow expected from cislunar plasma. To ameliorate this limitation, charged particle optics are utilized to expand and refocus the beam such that the beam is large enough to fully envelop an object and flow parallel to the chamber walls. This is referred to as telescoping the beam, as shown in Fig. 1. Spacecraft wake experiments have been conducted utilizing an expanding plasma source, so parallel ion flow is ideal but not a strict requirement. Charged particle optics involves manipulating the trajectory of charged particles by altering the ambient electric or magnetic field and has been a topic of study since the early 20th century, with several publications outlining the general concepts [39], [40], [41], [42]. Altering charged particle trajectories has been used to focus ion beams for mass spectrometry [43], [44], radiotherapy for cancer patients [45], sample etching and preparation [46], [47], investigating irradiation effects on materials [48], [49], and more. This study aims to expand this research by using ion optics, a subset of charged particle optics, to enable wake experiments. The results could also be extended to any experiment, in which it is beneficial to expand the installed ion gun's capability to manipulate the ion beam.

Electrostatic, magnetic, or a combination of the two types of lenses can be used to manipulate the ion beam as desired. Low energy ion (5 eV–50 keV) trajectories are generally altered more by varying electrostatic fields versus magnetic fields [40]. Furthermore, implementing simple electrostatic lenses allows for easy adaptability and implementation in other vacuum systems. Accordingly, electrostatic lenses held at constant potentials are designed and utilized to manipulate the ion beam.

The materials and methods used to characterize the ion beam and design the electrostatic lenses are presented in Section II. Electrostatic lens configuration results are discussed in Section III, and installation and characterization of the lenses are presented in Section IV. The lenses are used to generate a spacecraft ion wake in Section V. Finally, a review and conclusion are presented in Section VI.

II. Materials and Methods

A. Cislunar Plasma Experimental Representation

The wake experiment is limited by the experimental volume available in the ECLIPS chamber, which has a height of approximately 86 cm and a diameter of approximately 60 cm. The ion lenses are restricted to the top 50 cm of the chamber to leave sufficient room for experiments to be conducted. Despite the size of the ECLIPS chamber, large-scale phenomena can still be represented. A scaling law can be applied to relate the spacecraft's experimental radius R_0 to the radius in the environment of interest R_{sim} [50]

$$R_{\text{sim}} = \sqrt{\frac{n_i}{n_{\text{sim}}}} R_0 \tag{1}$$

where n_i is the experiment plasma density and n_{sim} is the environment plasma density. In other words, if the density of the experimental ion beam is larger than the environmental plasma density, the experimental object represents a larger spacecraft. This relationship was derived for LEO plasma-body interactions, but it applies to processes governed by the Vlasov-Maxwell equations [50]. Thus, this may be applied to cislunar plasma environments where spacecraft wake form. The density of the ions in the ECLIPS chamber is

$$n_i = \frac{I_{\text{beam}}}{q_e A v} = \frac{I_{\text{beam}}}{q_e \pi r^2} \sqrt{\frac{m_i}{2E}} \tag{2}$$

where I_{beam} is the ion gun current, q_e is the elementary charge in Coulombs, A is the final area of the beam, or πr^2, v is the

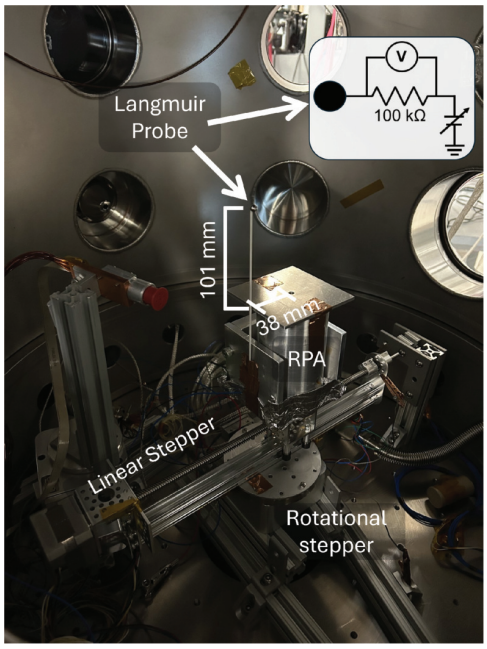

Fig. 2. Sensor package and LP circuit.

velocity of the ions, m_i is the mass of the ions, and E is the energy of the ions, found as $E = 1/2 m_i v^2$.

The argon ions (Ar^+) generated in the ECLIPS chamber are not representative of cislunar plasma environments, which are comprised mostly of hydrogen ions (H^+). Fortunately, there is another scaling law from [50] that can be used to relate the velocity of two different ion species

$$v_{\text{sim}} = \sqrt{\frac{m_i}{m_{\text{sim}}}} v \tag{3}$$

where v_{sim} is the velocity of the environment being simulated and m_{sim} is the mass of the ions in the simulated environment. Spacecraft wake form in the cislunar magnetosheath and solar wind regions, which have H^+ bulk velocities from 350 to 930 km/s [51]. Hydrogen ions with a bulk velocity of 400 km/s reasonably represent solar wind or magnetosheath conditions, which corresponds to Ar^+ ions with a velocity of 63.6 km/s or a beam energy E_B of approximately 835 eV. The beam is held at this energy in all simulations and experiments.

B. Ion Beam Characterization

A spherical LP and retarding potential analyzer (RPA) are used to take measurements of the ion beam at different positions, as shown in Fig. 2. The LP is constructed from a 2.5-mm radius aluminum sphere spot welded to nickel wire. The wire is electrically isolated and the probe is held in place with a ceramic tube. Before each experiment, the LP is bombarded with 3-keV ions, the highest energy possible with the ion gun, and held at −1 kV to remove surface contamination. A sweep outside the ion gun is then conducted to obtain measurements of the expected noise level or the load line. The load line is subtracted from the final measurements during analysis [52]. This noise is generally two orders of magnitude smaller than the measurements obtained in the ion gun. The LP is swept from 0 to −100 V in 10-V steps using

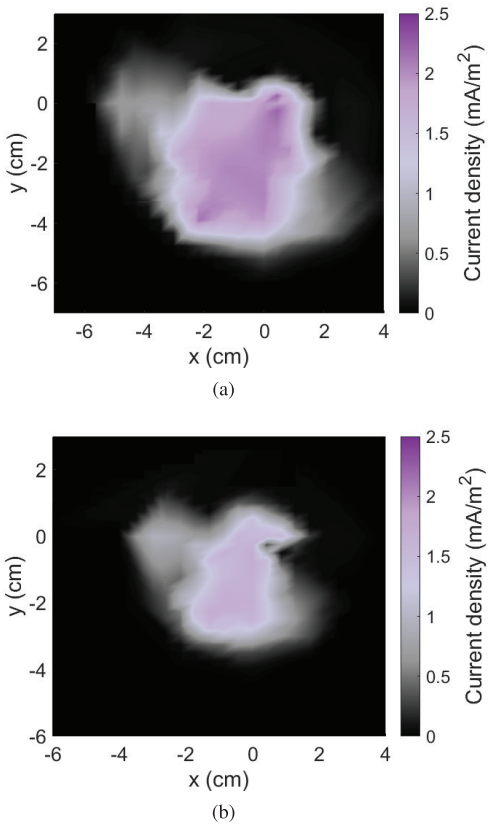

Fig. 3. Current density map of the unaltered ion gun emissions measured by (a) RPA measurements and (b) LP measurements.

a Matsusada AU-IR30 high-voltage power supply (HVPS), and the voltage change across a 100-kΩ resistor is measured using a Keithley DMM6500 multimeter. The voltage change is then converted into collected current using Ohm's Law ($V = IR$). It should be noted that the multimeter has an internal resistance of 20 MΩ, which is added to the circuit resistance when converting the measured change in potential to collected current. These measurements generate a current versus potential (I-V) curve in the ion saturation region [53]. The LP theory presented in [54] is implemented in MATLAB and utilized to obtain the ion current density results presented. The RPA was previously constructed from a Faraday cup with a front grounding grid followed by a biasing grid [55]. An aluminum sheet is placed in front of the RPA's entrance to decrease the entrance aperture to a circle with a radius of 2.4 mm. This makes the RPA entrance comparable to the size of the LP and allows for measurements to be taken in 5-mm steps. The RPA is located approximately 460 mm from the ion gun exit, and the LP is positioned approximately 101 mm higher than the RPA, or 359 mm from the ion gun. Both instruments are placed on a linear stepper motor capable of moving the sensors ±10 cm from the center of the chamber and a rotational stepper capable of rotating 360 °. This allows the entire space to be characterized with a resolution of 5 mm.

To determine if the ion beam is symmetrical and ensure the SIMION model is properly configured, a current density map of the ion beam is obtained, as shown in Fig. 3. The beam is not perfectly symmetric, but edge points can be used to

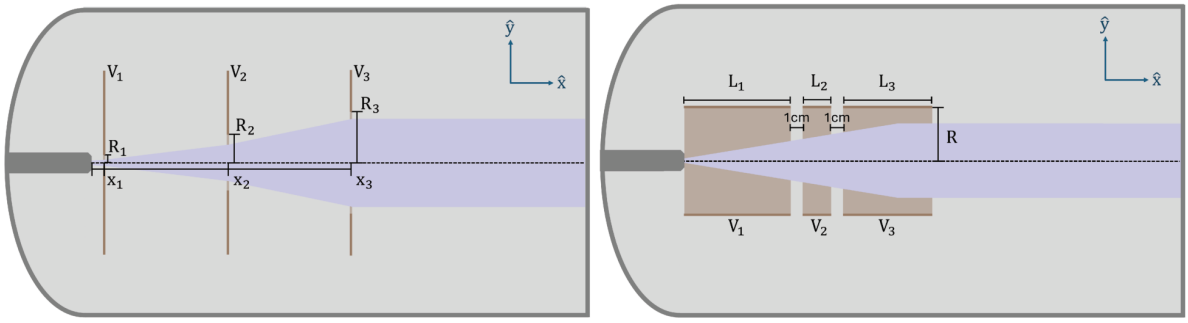

(a) (b)

Fig. 4. (a) Thin and (b) thick lens schematics.

determine an average beam radius. The average beam radius is 3.84 cm as measured by the RPA and 3.15 cm as measured by the LP. Based on this, and assuming an initial radius of 1 mm at the ion gun exit, the half-angle of the beam is estimated to be $\approx 4.9°$.

It is surprising that the current density measured by the LP is smaller than that measured by the RPA because the LP is located in a region of the beam with a smaller radius and higher current density. However, LPs are often stated to have an accuracy of 20%–50% of real values [53], [54], and contamination and secondary electrons emitted from the chamber and RPA can alter the current magnitude. Regardless, the magnitude of the current density measured by the LP does not change the results of this project because the edge points of the current measurements are used to determine the size of the beam. This process is further described in Section IV-A.

C. Particle Tracing and Optimization Framework

SIMION, a particle tracing software package used to calculate electric fields and trajectories of charged particles, is used to design and investigate the electrostatic lenses [56]. SIMION computes the trajectory of each charged particle from Newton's second law

$$\frac{d\mathbf{v}}{dt} = \frac{q}{m}\mathbf{E} \tag{4}$$

where $\mathbf{v}$, q, and m are the particle velocity, charge, and mass, respectively, $\mathbf{E}$ is the electric field, and t is the time. The electric field is derived from the electrostatic potential field V as follows:

$$\mathbf{E} = \nabla V \tag{5}$$

while V is computed by solving Laplace's equation

$$\nabla^2 V = 0 \tag{6}$$

in the simulation domain. SIMION employs a regular Cartesian mesh with boundary conditions determined by set potentials of each electrode (Dirichlet) or by the zero-derivative of the potential (Neumann). The grounded vacuum chamber wall is modeled and utilized as a 0-V Dirichlet boundary.

Three lens configurations are considered for installation in the ECLIPS vacuum chamber: two thin lenses, three thin lenses, and three thick lenses, as shown in Fig. 4. The thin lenses are flat, thin plates with openings of radius R_{lens} to allow the beam to pass through. The thick lenses are thin cylindrical shells that again allow the ion beam to pass through the center. Each thin lens has three parameters: location x_{lens}, electric potential V_{lens}, and inner radius R_{lens}. Each thick lens has a variable thickness L_{lens} and potential. The thick lenses all have the same radius, and the top of the first lens is in line with the ion gun opening. The final lens configuration can then have anywhere from six-to-nine variables.

To efficiently optimize the design of the lenses, a windows batch file is written to enable MATLAB to alter the lens parameters and run a SIMION simulation. Then, a genetic algorithm and fminsearch in MATLAB are used to minimize an associated cost function. A genetic algorithm is a method for solving constrained or unconstrained optimization problems based on a natural selection process that mimics biological evolution. The algorithm is proficient at finding the approximate absolute minimum for the entire problem space, but the solution is not as accurate as MATLAB's fminsearch. MATLAB's fminsearch is a nonlinear programming solver that finds the minimum of a specified function and is proficient at determining the local minimum near a defined starting point. Therefore, a genetic algorithm is first implemented, and then the results are used as the initial guess for fminsearch, optimizing the capabilities of both functions.

The goal of this study is to maximize the final radius of the beam and minimize the spread of the beam in the direction parallel with the ground of the chamber, which is defined as the y-direction. In addition, the lenses may accelerate the ions, so the difference between the final velocity and 63.6 km/s should be minimized. The cost function is then

$$\text{Cost} = w_y \frac{n}{y_{\max}^2} + w_{v_y}\text{sum}\left(v_y^2\right) + w_{v_x}\text{sum}\left((v_x - 63.6)^2\right) \tag{7}$$

where $y_{\max}$ is the maximum radius achieved by an ion particle, n is the number of particles flown, w_y is the weight applied to the final radius, v_y is the final velocity of each particle in the y-direction, w_{v_y} is the weight applied to minimizing the spread of the particles in the y-direction, v_x is the velocity of each particle in the x-direction, and w_{v_x} is the weight applied to minimizing the variance of the final velocity from the defined optimal velocity, 63.6 km/s. Only the maximum value of the radius component is used $y_{\max}$ because particles that impact near the center of the chamber have a minuscule final position in the y-direction, resulting in an uncharacteristically high-cost function. The velocity components of the cost function

TABLE I
LENS DESIGN CONSTRAINTS

Parameter	Constraints
E_B	825 eV $\leq E_B \leq$ 845 eV
V_{lens}	-30E3 V $\leq V_{lens} \leq$ 30E3 V
R_{lens}	$5 \leq R_{lens} \leq 250$ mm
x_{lens}	$x_3 \geq x_2+100$ mm $\geq x_1+100$ mm; $x_1 \geq 101$ mm; $x_2 \leq 500$ mm (2 thin lenses); $x_3 \leq 500$ mm (3 thin lenses)
L_{lens}	$L_1 + L_2 + L_3 \leq 380$ mm

sum the final velocity of all the particles, which creates higher values compared with the final position of a singular particle. Therefore, the radius component is multiplied by the number of particles to make the values of each component of the cost function comparable. In addition, if the potential of the lens is too high, the particles will be attracted back toward the lenses and impact them. To avoid this solution, the cost function is automatically given a value of 1E10 if the final position of the particles is not at the floor of the chamber.

The constraints must be selected such that the final lens design fits inside the available experimental area and is within the bounds of the technology available in the ECLIPS chamber. The beam energy E_B is allowed to vary $\pm$10 eV from the optimal energy in order to account for the change in velocity due to the lenses, and the possible potential of the lenses V_{lens} is constrained by the capabilities of the Matsusada AU-30R1 HVPS, $\pm$30 kV. The ion gun exit has a radius of 4 mm, so the radius of the space in the center of the lenses R_{lens} is set to a minimum of 5 mm to ensure that the lens do not block the opening. The maximum radius is 250 mm to allow space for stands to be installed on the outside of the lenses. The ion gun is 100-mm long, and the lenses must be placed in the top 500 mm of the chamber to leave space for wake experiments to be conducted. For the thin lenses, this means the lens locations x_{lens} must be greater than 100 mm and less than 500 mm. The thick lenses have set separation distances of 100 mm, so the combined length of the lenses L_{lens} must be less than 380 mm. These constraints are shown in Table I.

III. OPTIMIZATION RESULTS

Following the evaluation done in Section II-B, the half-angle is set to 4.9°. In the process of performing the lens design optimization and modifying the weights of each component of the cost function, it is found that the lenses negligibly change the energy of the ion beam. Therefore, w_{v_x} is set to 0, as this component does not impact the results. Furthermore, determining the proper w_y and w_{v_y} weights to telescope the beam such that each component is evenly prioritized is found to be nonintuitive, and it is inefficient to readjust the weights because each optimization process takes approximately 16 hours. Instead, the cost function is set to solely maximize the final radius of the beam ($w_y = 1$ and $w_{v_y} = 0$), and adjustments are made postoptimization to minimize the final particle velocities in the y-direction.

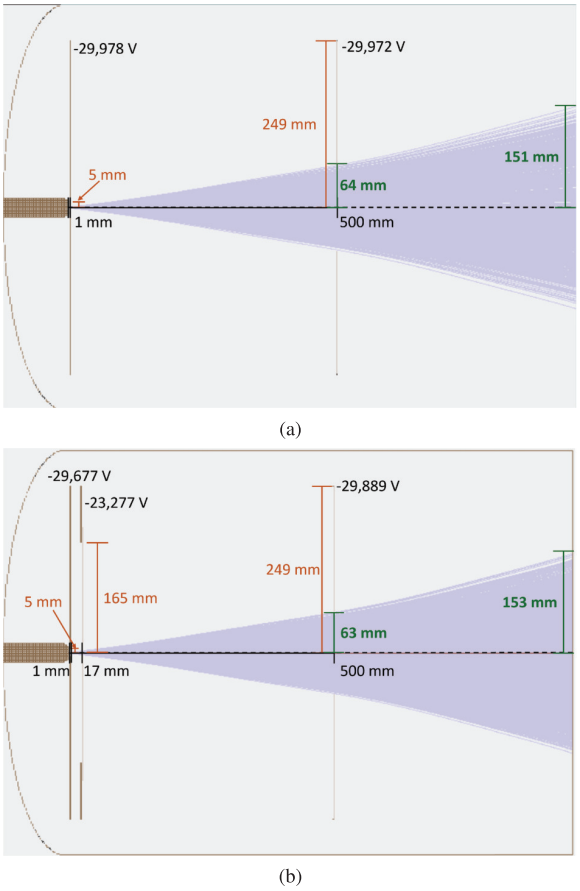

Fig. 5. Optimization results for (a) two thin lenses and (b) three thin lenses. Lens radii values are shown in orange, lens potential, and placement values in black, and beam radii values in green.

A. Thin Lens Results

The optimization results for two and three thin lenses are shown in Fig. 5. Interestingly, there is negligible difference between using two or three thin lenses. Both designs create a beam radius of 153–154 mm at the bottom of the chamber and a beam radius of 63 at 500 mm, the maximum lens x-value. In fact, the result for three thin lenses places the middle lens 1.6 cm from the first lens at a similar potential, and it is found that removing this lens does not change the beam properties. Therefore, both solutions functionally use two thin lenses to expand the beam. In both designs, the first lens is as close to the ion gun as possible with the smallest radius possible and is held at nearly the maximum potential. The second lens is then placed at the maximum distance from the ion gun, the lens radius is as large as possible, and the potential is again nearly the maximum possible value. This process appears to provide an initial increase in beam radius as the ions are exiting the ion gun and a final boost to the radius as far as possible from the beam's point of origin.

Because the cost function is designed to simply maximize the beam radius, the resulting beam is not telescoped as desired. Therefore, the second lens is modified to telescope the

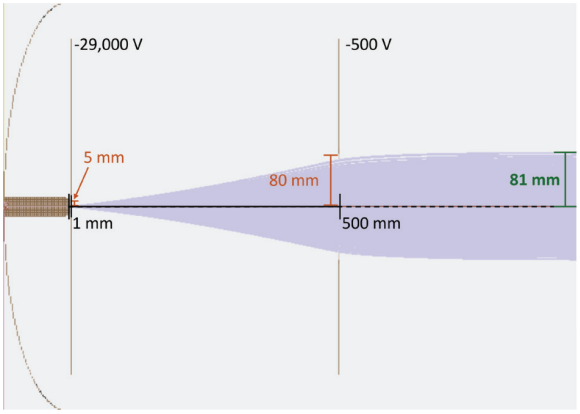

Fig. 6. Telescoped beam with thin lenses. Lens radii values are shown in orange, lens potential, and placement values in black, and beam radii values in green.

beam. It is found that with an initial lens at −29000 V, a second lens at 500 mm at −500 V with an 8-cm radius telescopes the beam, as shown in Fig. 6. The final beam radius is then 81 mm, over twice as large as the unaltered beam radius found in Section II-B. For this lens design, the lens closest to the ion gun expands the beam and is referred to as the *expanding lens*. The lens farthest from the ion gun refocuses the beam and is referred to as the *focusing lens*.

B. Thick Lenses Results

The optimization results for the thick lens design are shown in Fig. 7. Initially, the thick lenses widen the beam by expanding it with a negative lens. Then, two positive lenses repel the beam to such an extent that the ions cross through a point and the polarity of the velocity in the y-direction v_y is flipped. This generates a beam with a final radius of 142 mm, approximately a centimeter smaller than the radius achieved by the thin lenses. The process of widening the beam is more complex than previously found, which may create issues when characterizing spacecraft wake formations. Therefore, the lens potentials are restricted such that the beam is widened without the ion paths crossing each other. To do so, the first lens must be negative ($V_1 \leq 0$), and the last two lenses are also negative with potential magnitudes greater than one-tenth the magnitude of the first lens potential ($V_2 \leq 0.1V_1$ and $V_3 \leq 0.1V_1$). The resulting lens design negligibly changes the radius of the beam, indicating that the thick lens design is not viable for increasing the radius of the beam without the ion trajectories crossing. Because the thick lens design is not as effective at increasing the beam radius as the thin lens design, the thin lens design with an expanding and focusing lens is selected to alter the ion beam.

C. Arcing Analysis

A thin expanding lens placed as close as possible to the ion gun is optimal for increasing the radius of the beam. However, the high-voltage lens may arc with the nearby, grounded ion gun. If arcing occurs, the HVPS will shut off and the ion gun may be damaged. To prevent this, the maximum voltage that can be achieved before arcing is characterized at several

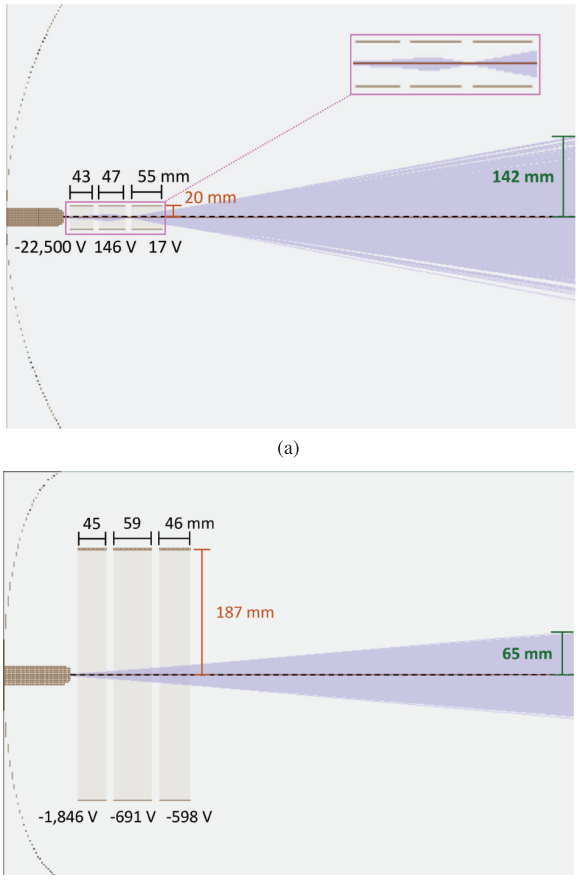

Fig. 7. Optimization results for thick lens design. (a) Initial results (top) utilize constraints shown in Table I and (b) restricted (bottom) has the additional constraints $V_1 \leq 0$, $V_2 \leq 0.1V_1$, and $V_3 \leq 0.1V_1$.

separation distances. This is accomplished using two conductive sheets of aluminum that are held at the desired separation distance. One sheet is grounded, and the voltage on the second sheet is increased until arcing occurs. The arcing potential is then recorded, the separation distance is increased, and the experiment is repeated. The wake experiment is conducted in a vacuum, but the arcing voltage versus separation distance is recorded in the atmosphere, which is approximately 630 torr at room temperature in Boulder, CO, USA. This is done because the objects may arc through the flowing argon, resulting in lower possible potentials at a set separation distance than expected in a vacuum. The arcing voltage versus separation distance is plotted as a white line over the expected final beam radius versus lens distance from the ion gun and lens potential in Fig. 8. This line indicates where the lens may be expected to arc with the ion gun, and safe lens voltage and distance combinations are located below the white line. Fortunately, it is found that the beam radius plateaus after a certain lens potential, which means lower expanding lens potentials than found in Section III-A can be used to achieve the maximum beam radius. It is evident from the figure that the largest beam radius at the RPA is limited to 60–70 mm for a lens located 3–5 mm from the ion gun. Once the lens is placed 6 mm or more from the ion gun exit, the radius of the beam is negligibly increased.

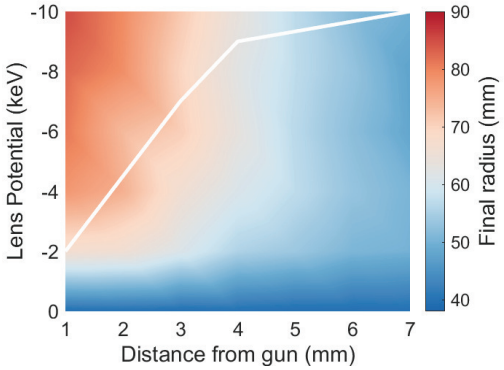

Fig. 8. Expected beam radius at the RPA position (46 cm from ion gun exit) versus expanding lens potential and distance from ion gun. The white line indicates the voltage and distance combination at which arcing may occur.

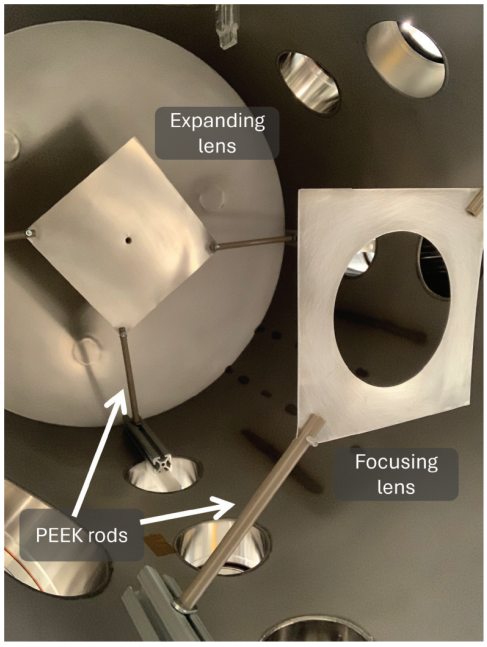

Fig. 9. Lens setup in the ECLIPS vacuum chamber.

IV. Lens Characterization

The lenses are constructed from 6-mm-thick sheets of aluminum and held at the desired potentials using Matsusada AU-30R1 HVPS. PEEK rods are used to electrically isolate the lenses from the chamber walls and hold them in place, as shown in Fig. 9. The lenses are sanded to avoid any irregularities on the surface or edges, and a level is used to ensure they are as flat as possible upon installation. As described in Section III, the optimal lens design uses an expanding lens near the ion gun exit and a focusing lens farther away to telescope the beam. Before combining the entire setup, the expanding and focusing lenses are installed one at a time and measured to test their individual effects.

A. Expanding Lens

The expanding lens is positioned 5 mm from the ion gun exit with an inner radius of 5 mm. Creating a detailed map of the lens, as done in Section II-B, takes approximately 4 h. It is desirable to test the entire range of lens potentials in the same sitting, as this minimizes changes to the setup or ion beam properties. Therefore, a faster method of estimating the size of the beam must be determined. The general shape of the beam is assumed to be approximately circular. Then, at least three edge points of the beam are found and the positions are recorded as Cartesian coordinates (x, y). These points are then used to find the center point of the beam (x_c, y_c) and radius r by performing a linear least squares (LLS) fitting to the equation of a circle

$$r^2 = (x - x_c)^2 + (y - y_c)^2 . \tag{8}$$

To find these edge points, the sensors measure a straight line along the entire length of the stepper motor, then the rotational stepper motor is rotated 90 °, and the process is repeated. This results in three-to-four edge points being recorded and utilized to determine the position and size of the circular projection of the beam. Examples of these circular projections of the beam are shown in Fig. 10. Based on the RPA measurements, it is also found that the final ion energy remains at approximately 835 eV. This validates the SIMION results, which indicated that the lenses are not expected to significantly change the ion energy.

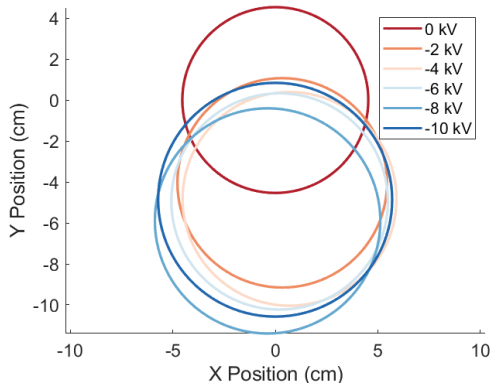

Fig. 10. Projections of the ion beam made from RPA measurements for varying expanding lens potentials.

As shown in these projections, the beam is expanded and *translated* as the potential is varied. This indicates that the lens is misaligned, meaning it is not perfectly flat or centered with respect to the ion gun. Misalignment is expected within the system, particularly because this lens design is intended to be installed by hand and adaptable to different vacuum chamber systems. Therefore, the beam translations are characterized by various misalignment.

The expanding lens is modeled in SIMION at a distance of 5 mm from the ion gun to match the experimental setup. The simulated lens is then shifted from the center of the simulation and tilted to characterize how the misalignment may impact the ion beam radii and offset. The translation, or offset, of the beam and final radius values for various lens misalignments, is shown in Fig. 11. The dashed lines display results for a perfectly centered but tilted beam and the solid lines represent an off-center but perfectly level lens. Tilting the lens has a significantly smaller effect than shifting the lens with respect to the ion gun. Thus, any ion beam translations are contributed to an off-center lens.

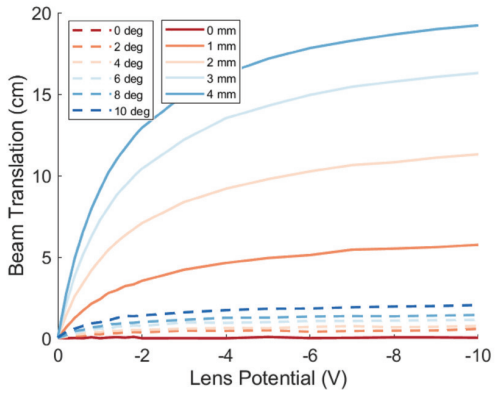

Fig. 11. SIMION simulations of ion beam translation at the RPA position versus expanding lens potential for varying misalignments. Solid lines indicate an off-center lens and dashed indicate a tilted lens.

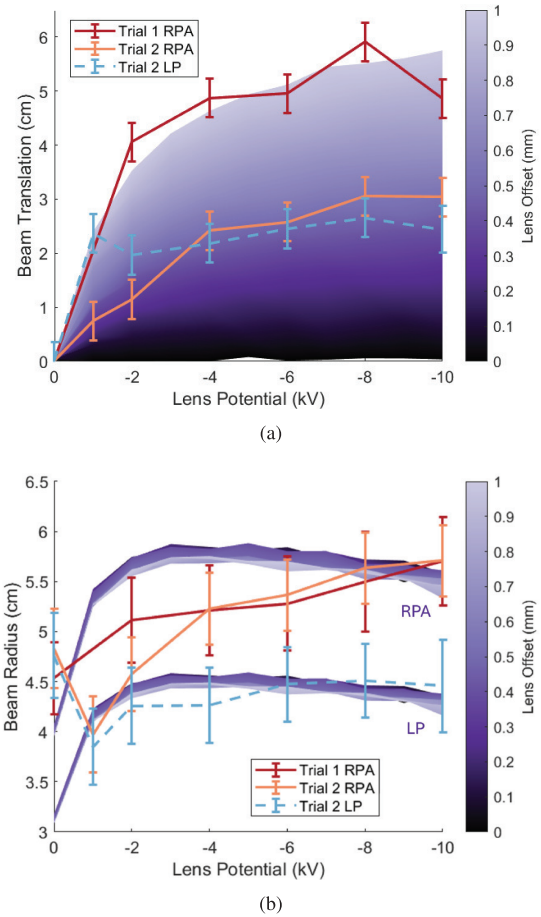

Fig. 12. Ion beam (a) translation (top) and (b) radius (bottom) versus expanding lens potential. SIMION results are shown in a purple gradient. Trial 1 is estimated to be shifted 0.9 mm and Trial 2 is estimated to be shifted 0.5 mm.

The expanding lens was set up and characterized in two separate trials. The translation of the lenses is unknown, so the recorded results are compared with SIMION results to estimate how much the lenses might have been offset. The experimental and corresponding SIMION results for the two trials are shown in Fig. 12. The error bars indicate the 1σ value from the LLS fitting and an assumed measurement error of ± 2.5 mm. The beam translation is only shown at the RPA position because the translation between the RPA and LP positions changes by millimeters. Therefore, the SIMION results have significant overlap, and showing both results is redundant. The LP was improperly connected to the multimeter during trial 1, so there are no LP results for that test. It is estimated that trial 1 was offset approximately 0.9 mm and trial 2 was offset 0.5 mm. The experimental and SIMION beam translations correspond well with each other. This validates that the translation of the beam can be contributed to the lens being off-center with respect to the ion gun by submillimeter magnitudes.

SIMION shows a quick jump in radius before a plateau, while the experimental results indicate a more gradual increase in radius and then a plateau. This may be due to inaccuracies in the chamber model in SIMION, as some unmodeled components, such as the chamber windows or wires may slightly alter the potential fields. However, it is shown that the radius of the beam is increasing with lens potential, the majority of the SIMION results are within the error bounds of the experimental results, and the maximum radius for both appears to be approximately the same. Thus, the expanding lens is performing as designed and generating a wider beam as predicted.

B. Focusing Lens

In order for the focusing lens to "compress" the ions into a smaller radius beam, the lens must be more positive than the preceding lens or ion source [39]. In initial experiments using the focusing lens, the lens is placed 36 cm down from the ion gun exit and has an opening of 50 mm. The LP is then located 1.6 cm from the lens, and the RPA entrance is 11.6 cm from the lens. Experiments revealed that the proximity of the LP to the focusing lens significantly alters the electric field and resulting measurements. This phenomenon was recreated in SIMION, and comparisons between current density measurements modeled in SIMION and measured in experiments show good agreement. This is described in further detail in [57]. However, phenomena, such as beam deflection may be missed if the current density is solely used to evaluate the beam behavior. Therefore, the experiments are modified and repeated. The LP is shifted down so it is only 58 mm above the RPA entrance compared with 101 mm. The focusing lens is widened to a 70-mm radius and moved to 31 cm below the ion gun exit. This creates a separation distance of 10.5 cm between the lens and LP.

The beam translation is characterized for this lens configuration, as shown in Fig. 13. Once again, an off-center lens translates the beam more than a tilted lens. Since the lens is farther from the ion source, lens translations on the order of centimeters are required to generate beam translations comparable to those seen in Section IV-A. This is useful because the focusing lens is farther from the ion gun, and the vacuum chamber walls prevent the focusing lens and ion gun from being seen at the same time. As a result, the focusing lens is aligned to the bottom of the vacuum chamber using a vertical laser level. The floor of the vacuum chamber is not connected to the top of the vacuum chamber, and shifts in the

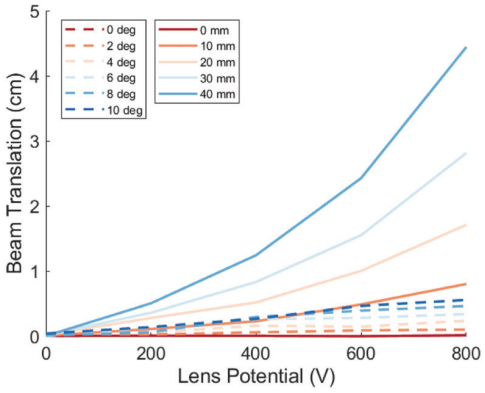

Fig. 13. SIMION simulations of ion beam translation at the RPA position versus lens potential for varying focusing lens misalignments. Solid lines indicate an off-center lens and dashed indicate a tilted lens.

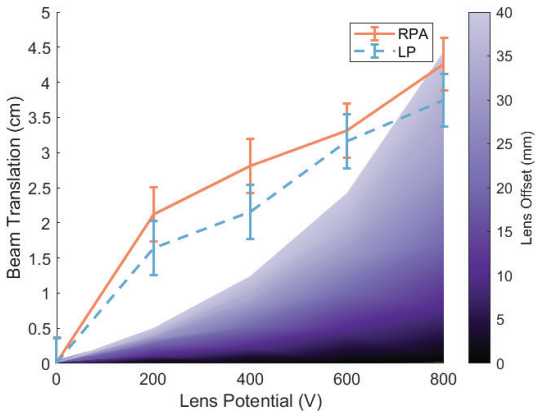

(a)

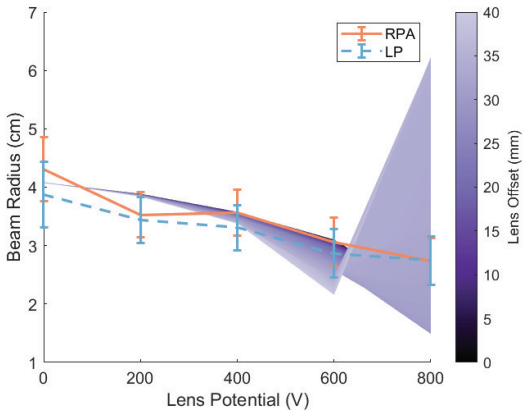

(b)

Fig. 14. Ion beam (a) translation (top) and (b) radius (bottom) versus focusing lens potential. SIMION simulation results are shown in a purple gradient, and it is estimated the lens is offset ≈ 34 mm.

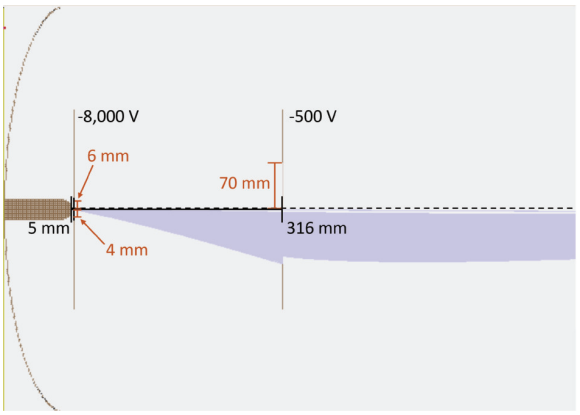

(a)

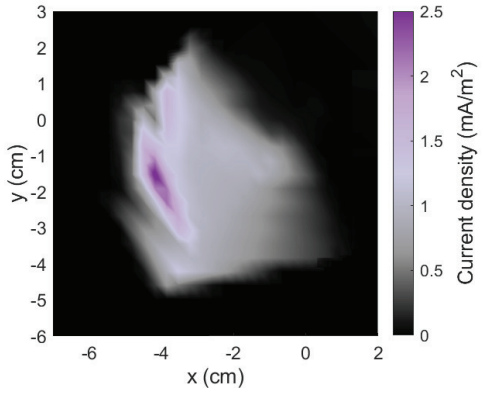

(b)

Fig. 15. Current density map measured by the LP with the expanding and focusing lens in place (bottom) and an SIMION simulation of a possible corresponding lens setup (top). (a) SIMION. (b) Experiment.

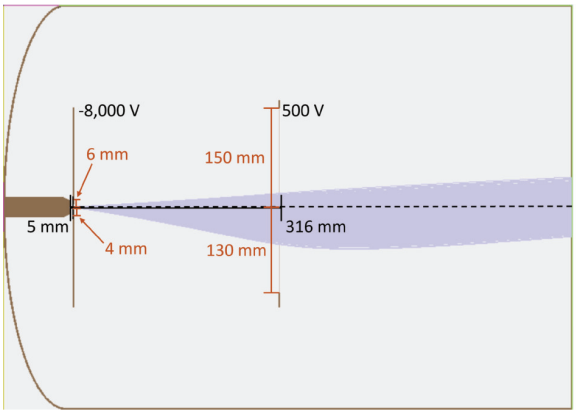

Fig. 16. SIMION simulation of both lenses installed with expanding lens off-center by 1 mm and focusing lens off-center by 1 cm.

vacuum chamber floor cause additional misalignment between the ion gun and the focusing lens.

At the defined the lens configuration, the beam is estimated to be telescoped for a lens potential of 600 V. The beam radius and offset versus lens potential are shown in Fig. 14, and the SIMION results are shown in the background as a purple gradient. As with the expanding lens, the error bars indicate the σ value from the LLS fitting and an assumed measurement error of ± 2.5 mm. The ion energy is also again measured at approximately 835 eV by the RPA. The SIMION results are shown at the RPA location. The beam radius decreases as the lens potential increases, as expected, and the beam is translated 4.25 cm for an 800 V lens. Based on this, it is estimated that the beam is off-center by approximately 3.4 cm. SIMION simulations indicate that if the beam is more off-center than this, at approximately 800 V, the lens significantly repels the nearby beam and begins to expand the beam radius. The experimental results indicate the beam is translated approximately 1 cm more than indicated by the

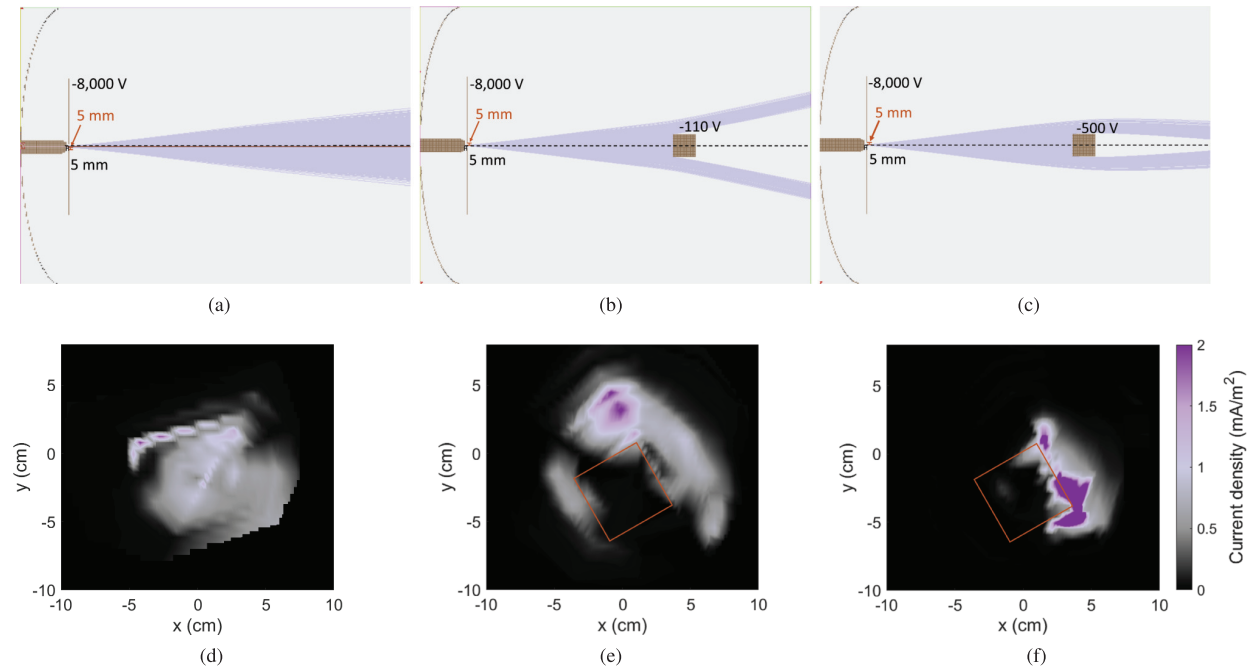

Fig. 17. SIMION simulation of chamber wake generation (top) and current density maps of experimentally generated wakes (bottom). A projection of the cube is shown in orange. (a) and (d) No cube. (b) and (e) −110-V cube. (c) and (f) −500-V cube.

SIMION simulations for a lens offset of 3.4 cm. However, the beam radius decreases as expected, so it is unlikely the lens is more off-center. It is possible that the wires providing power to the focusing lens and stepper motors alter the electric field and generate more beam translation than predicted. The beam radius versus lens potential results show good agreement with the SIMION simulations, and the SIMION results are within the 1σ error bars of the experimental results. This, in addition to the focusing lens results presented in [57] validate that the beam is focused as predicted and can reasonably be assumed to be telescoped at 600 V.

C. Both Lenses

Finally, both lenses are installed. The expanding lens is kept 5 mm from the ion gun exit with a radius of 5 mm, and the focusing lens is kept 36 cm from the ion gun exit with a radius of 7 cm. This should leave 3 cm of space between the ion beam edge and the focusing lens opening. The lens should be telescoped, similar to the beam shown in Fig. 6, with a final radius of 45 mm when the expanding lens is held at −8 kV and focusing lens is held at −500 V. The current density map measured by LP is shown in Fig. 15(b). Here, it appears the beam impacts the edge of the focusing lens, as shown by the curvature on the left side of the plot. It is difficult to determine if one or both lens misalignments causes this, but upon investigating with SIMION, it is found that in this configuration if the expanding lens is off-center by 1 mm, the beam will impact the focusing lens, as shown in Fig. 15(a). The focusing lens is also likely off-center, likely increasing the percentage of the ion beam that is impacting the lens.

A larger focusing lens could be utilized to avoid the beam impacting the lens. However, the lenses are not installed with submillimeter precision and misalignment will still be expected. A SIMION simulation with a larger focusing lens and realistic lens placements, or the expanding lens off-center by 0.5 mm and focusing lens off-center by 1 cm, is shown in Fig. 16. The larger focusing lens does allow the beam to pass through without impact. However, the combined misalignments of the lenses cause the beam to have a nonzero velocity parallel to the floor of the chamber. In other words, the focusing lens does not cause the ions to flow parallel to the chamber walls and represent solar wind flow in the cislunar region. This could be useful if it is desirable to simulate a spacecraft with a velocity comparable with the plasma bulk velocity ($v_{sc} \approx v_{bulk}$) traveling in a direction that is not parallel to the bulk velocity, such as the conditions experienced by the Parker Solar Probe [27]. For this project, the aim is to represent solar wind flow around the cislunar spacecraft, and the spacecraft velocity is not comparable to the bulk velocity, so ion flow parallel to the chamber walls best represents the ion wake around a cislunar spacecraft.

V. Wake Generation

The goal of this project is to generate a wake that can be used in future touchless potential experiments. In this future experiment, the electron and ion trajectories will be characterized both with and without an electron beam and spacecraft wake present. To accomplish this, as previously mentioned, the beam must be large enough to fully envelop a representative spacecraft and be measured, and ideally, the ions would flow parallel to the chamber walls. Since the focusing lens introduces additional deflections and does not generate ion velocities that represent cislunar plasma flow, only the expanding lens is used to generate representative spacecraft wakes. This also generates a larger beam around the representative spacecraft, making the wake formation simpler to characterize.

The expanding lens is again held 5 mm from the ion gun exit, has an inner radius of 5 mm, and is held at a potential of −8 kV. Therefore, the beam radius at the representative spacecraft location should be approximately 5.5 cm, which is large enough to fully envelope a representative spacecraft. A cube with a width of 5 cm is used to represent a spacecraft. Assuming a beam current of 10 μA, representative solar wind plasma density of 6E6 m^{-3}, and using (1) and (2), the 5-cm cube represents a spacecraft with a width of 6.6 m.

As described in Section IV-A, if the expanding lens is off-center by submillimeter distances, the beam is deflected by several centimeters. Therefore, the expanding lens is first installed and the position of the beam is determined without the cube in place. Then, the vacuum chamber is opened, the cube is placed in the path of the beam, and the experiment is repeated with the cube in the beam path. The RPA cannot fit underneath the cube in the vacuum chamber, so only the LP is used to determine the ion beam behavior. The expected ion beam behavior and experimental results are shown in Fig. 17. It is expected that a −110-V cube creates an expanding wake that is larger than the width of the cube. This is found experimentally, as the width of the beam is larger with the −110-V cube in place versus without. When the cube potential is increased to −500 V, the ions are attracted toward the cube, and a closing wake is generated. This is again found in experiments, as the width of the beam is the smallest for this configuration. The ions seem to disappear on the left side of the cube when the voltage is decreased from −110 to −500 V. This likely occurs because the ion beam is thinner on this side, and the ions are attracted into the side of the cube when the voltage magnitude is increased. Overall, it is shown that the expanding lens can be used to reliably expand and translate the beam, and the wake behavior matches in simulations and experiments.

VI. Conclusion

Electrostatic lens configurations are designed and used to manipulate ion beam parameters in a vacuum chamber. It is found that two thin lenses are optimal for increasing the radius of the beam and telescoping the beam. When telescoping the beam, the top lens is referred to as the expanding lens, and the bottom is referred to as the focusing lens. If the expanding lens is off-center by submillimeter distances, the ion beam is deflected several centimeters. For the focusing lens, offsets on the order of centimeters deflect the beam several centimeters. Regardless, individually, both the expanding lens and focusing lens alter the ion beam radius as expected.

Spacecraft ion wakes are generated with only the expanding lens in place because maximizing the beam radius is deemed more important than focusing the flow of the ions. It is shown that wake formations around a cube with varying potential can be generated and measured, and the measured results show good agreement with simulations. Thus, electrostatic lenses are successfully designed, tested, and used to generate spacecraft ion wakes. This lens configuration could be implemented in any scenario in which it is necessary to widen, focus, or translate a beam with charged particles.

Acknowledgment

The authors would like to thank Leya Shaw for her help in troubleshooting and installing the electrostatic lenses.

References

[1] M. Bengtson, J. Hughes, and H. Schaub, "Prospects and challenges for touchless sensing of spacecraft electrostatic potential using electrons," *IEEE Trans. Plasma Sci.*, vol. 47, no. 8, pp. 3673–3681, Aug. 2019.

[2] M. T. Bengtson, K. T. Wilson, and H. Schaub, "Experimental results of electron method for remote spacecraft charge sensing," *Space Weather*, vol. 18, no. 3, pp. 1–12, Mar. 2020.

[3] M. T. Bengtson and H. Schaub, "Electron-based touchless potential sensing of shape primitives and differentially-charged spacecraft," *J. Spacecraft Rockets*, vol. 58, no. 6, pp. 1847–1857, Nov. 2021.

[4] Á. Romero-Calvo, J. Hammerl, M. Bengtson, and H. Schaub, "Touchless potential sensing of complex differentially-charged shapes using secondary electrons," *AIAA J. Spacecraft Rockets*, vol. 59, no. 5, pp. 1623–1633, Sep. 2022.

[5] K. Wilson and H. Schaub, "X-ray spectroscopy for electrostatic potential and material determination of space objects," *IEEE Trans. Plasma Sci.*, vol. 47, no. 8, pp. 3858–3866, Aug. 2019.

[6] K. Wilson, M. Bengtson, and H. Schaub, "X-ray spectroscopic determination of electrostatic potential and material composition for spacecraft: Experimental results," *Space Weather*, vol. 18, no. 4, Feb. 2020, Art. no. e2019SW002342.

[7] K. Wilson, J. Hammerl, and H. Schaub, "Using plasma-induced X-ray emission to estimate electrostatic potentials on nearby space objects," *J. Spacecraft Rockets*, vol. 59, no. 4, pp. 1402–1405, Jul. 2022.

[8] J. Hammerl, A. López, Á. Romero-Calvo, and H. Schaub, "Touchless potential sensing of differentially charged spacecraft using X-rays," *J. Spacecraft Rockets*, vol. 60, no. 2, pp. 648–658, Mar. 2023.

[9] Á. Romero-Calvo, K. Champion, and H. Schaub, "Enabling ultraviolet lasers for touchless spacecraft potential sensing," *IEEE Trans. Plasma Sci.*, vol. 51, no. 9, pp. 2468–2481, Sep. 2023.

[10] E. A. Hogan and H. Schaub, "Impacts of tug and debris sizes on electrostatic tractor charging performance," *Adv. Space Res.*, vol. 55, no. 2, pp. 630–638, Jan. 2015.

[11] E. A. Hogan and H. Schaub, "Impacts of hot space plasma and ion beam emission on electrostatic tractor performance," *IEEE Trans. Plasma Sci.*, vol. 43, no. 9, pp. 3115–3129, Sep. 2015.

[12] M. Bengtson, K. Wilson, J. Hughes, and H. Schaub, "Survey of the electrostatic tractor research for reorbiting passive GEO space objects," *Astrodynamics*, vol. 2, no. 4, pp. 291–305, Dec. 2018.

[13] J. A. Hughes and H. Schaub, "Electrostatic tractor analysis using a measured flux model," *J. Spacecraft Rockets*, vol. 57, no. 2, pp. 207–216, Mar. 2020.

[14] J. Hammerl and H. Schaub, "Effects of electric potential uncertainty on electrostatic tractor relative motion control equilibria," *J. Spacecraft Rockets*, vol. 59, no. 2, pp. 552–562, Mar. 2022.

[15] T. Bennett, D. Stevenson, E. Hogan, L. McManus, and H. Schaub, "Prospects and challenges of touchless debris despinning using electrostatics," *Adv. Space Res.*, vol. 56, no. 3, pp. 557–568, Aug. 2015.

[16] T. Bennett and H. Schaub, "Contactless electrostatic detumbling of axisymmetric GEO objects with nominal pushing or pulling," *Adv. Space Res.*, vol. 62, no. 11, pp. 2977–2987, Dec. 2018.

[17] V. Aslanov and H. Schaub, "Detumbling attitude control analysis considering an electrostatic pusher configuration," *J. Guid., Control, Dyn.*, vol. 42, no. 4, pp. 900–909, Apr. 2019.

[18] F. Casale, H. Schaub, and J. D. Biggs, "Lyapunov optimal touchless electrostatic detumbling of space debris in GEO using a surface multisphere model," *J. Spacecraft Rockets*, vol. 58, no. 3, pp. 764–778, May 2021.

[19] S. T. Lai, *Fundamentals of Spacecraft Charging: Spacecraft Interactions With Space Plasmas*. Princeton, NJ, USA: Princeton Univ. Press, 2012.

[20] M. J. Mandell, V. A. Davis, D. L. Cooke, A. T. Wheelock, and C. J. Roth, "Nascap-2k spacecraft charging code overview," *IEEE Trans. Plasma Sci.*, vol. 34, no. 5, pp. 2084–2093, Oct. 2006.

[21] B. Thiébault et al., "SPIS 5.1: An innovative approach for spacecraft plasma modeling," *IEEE Trans. Plasma Sci.*, vol. 43, no. 9, pp. 2782–2788, Sep. 2015.

[22] J. Wang and D. E. Hastings, "Ionospheric plasma flow over large high-voltage space platforms. I: Ion-plasma–time scale interactions of a plate at zero angle of attack," *Phys. Fluids B, Plasma Phys.*, vol. 4, no. 6, pp. 1597–1614, Jun. 1992.

[23] J. Wang and D. E. Hastings, "Ionospheric plasma flow over large high-voltage space platforms. II: The formation and structure of plasma wake," *Phys. Fluids B, Plasma Phys.*, vol. 4, no. 6, pp. 1615–1629, Jun. 1992.
[24] Y. Hu and J. Wang, "Plasma wake simulation for charged space platforms: Fully kinetic PIC versus hybrid PIC," *IEEE Trans. Plasma Sci.*, vol. 47, no. 8, pp. 3731–3738, Aug. 2019.
[25] N. Ahmad, H. Usui, and Y. Miyake, "The particle-in-cell simulation on LEO spacecraft charging and the wake structure using EMSES," *J. Adv. Simul. Sci. Eng.*, vol. 6, no. 1, pp. 21–31, 2019.
[26] W. J. Miloch, V. V. Yaroshenko, S. V. Vladimirov, H. L. Pécseli, and J. Trulsen, "Spacecraft charging in flowing plasmas; numerical simulations," *J. Phys., Conf. Ser.*, vol. 370, Jun. 2012, Art. no. 012004.
[27] R. E. Ergun et al., "Spacecraft charging and ion wake formation in the near-sun environment," *Phys. Plasmas*, vol. 17, no. 7, Jul. 2010, Art. no. 072903, doi: 10.1063/1.3457484.
[28] J. Wang, P. Leung, H. Garrett, and G. Murphy, "Multibody-plasma interactions-charging in the wake," *J. Spacecraft Rockets*, vol. 31, no. 5, pp. 889–894, 1994.
[29] A. Sjogren, A. I. Eriksson, and C. M. Cully, "Simulation of potential measurements around a photoemitting spacecraft in a flowing plasma," *IEEE Trans. Plasma Sci.*, vol. 40, no. 4, pp. 1257–1261, Apr. 2012.
[30] Y. Miyake, C. M. Cully, H. Usui, and H. Nakashima, "Plasma particle simulations of wake formation behind a spacecraft with thin wire booms," *J. Geophys. Res., Space Phys.*, vol. 118, no. 9, pp. 5681–5694, Sep. 2013.
[31] J. Maxwell and H. Schaub, "Low Earth orbit plasma wake shaping and applications to on-orbit proximity operations," *IEEE Trans. Plasma Sci.*, vol. 47, no. 10, pp. 4760–4769, Oct. 2019.
[32] W. A. Oran, U. Samir, N. H. Stone, and E. G. Fontheeim, "Laboratory observations of electron temperature in the wake of a sphere in a streaming plasma," *Planet. Space Sci.*, vol. 23, no. 7, pp. 1081–1083, Jul. 1975.
[33] S. Raychaudhuri, J. Hill, H. Y. Chang, E. K. Tsikis, and K. E. Lonngren, "An experiment on the plasma expansion into a wake," *Phys. Fluids*, vol. 29, no. 1, pp. 289–293, Jan. 1986, doi: 10.1063/1.865994.
[34] K. R. Svencs and J. Trøim, "Laboratory simulation of vehicle-plasma interaction in low Earth orbit," *Planet. Space Sci.*, vol. 42, no. 1, pp. 81–94, Jan. 1994.
[35] S. D. Hester and A. A. Sonin, "A laboratory study of the wakes of ionospheric satellites," *AIAA J.*, vol. 8, no. 6, pp. 1090–1098, Jun. 1970.
[36] C. L. Enloe, D. L. Cooke, S. Meassick, C. H. Chan, and M. F. Tautz, "Ion collection in a spacecraft wake: Laboratory simulations," *J. Geophys. Res., Space Phys.*, vol. 98, no. 8, pp. 13635–13644, Aug. 1993.
[37] R. Biasca and J. Wang, "Ion current collection in spacecraft wakes," *Phys. Plasmas*, vol. 2, no. 1, pp. 280–288, Jan. 1995, doi: 10.1063/1.871098.
[38] W. Yu, J. Wang, and K. Chou, "Laboratory measurement of lunar regolith simulant surface charging in a localized plasma wake," *IEEE Trans. Plasma Sci.*, vol. 43, no. 12, pp. 4175–4181, Dec. 2015.
[39] H. Liebl, *Applied Charged Particle Optics*. Cham, Switzerland: Springer, 2008.
[40] I. Drummond, "The ion optics of low-energy ion beams," *Vacuum*, vol. 34, nos. 1–2, pp. 51–61, 1984.
[41] M. Szilagyi, *Electron and Ion Optics*. Cham, Switzerland: Springer, 2012.
[42] P. Dahl, *Introduction to Electron and Ion Optics*. Amsterdam, The Netherlands: Elsevier, 2012.
[43] H. Wollnik, "Ion optics in mass spectrometers," *J. Mass Spectrometry*, vol. 34, no. 10, pp. 991–1006, Oct. 1999.
[44] T. W. Burgoyne and G. M. Hieftje, "An introduction to ion optics for the mass spectrograph," *Mass Spectrometry Rev.*, vol. 15, no. 4, pp. 241–259, 1996.
[45] C. Baker and R. Bingham, "Plasma lens for ion-beam focusing," in *Proc. APS Division Plasma Phys. Meeting Abstr.*, 2023, pp. 3–9.
[46] R. M. Langford, A. K. Petford-Long, and P. Gnauck, "Focused ion beam based sample preparation techniques," *Microsc. Microanalysis*, vol. 8, no. 2, pp. 46–47, Aug. 2002.
[47] M. Schaffer, J. Mahamid, B. D. Engel, T. Laugks, W. Baumeister, and J. M. Plitzko, "Optimized cryo-focused ion beam sample preparation aimed at in situ structural studies of membrane proteins," *J. Struct. Biol.*, vol. 197, no. 2, pp. 73–82, Feb. 2017.
[48] Y. Zhang et al., "New ion beam materials laboratory for materials modification and irradiation effects research," *Nucl. Instrum. Methods Phys. Res. B, Beam Interact. Mater. At.*, vol. 338, pp. 19–30, Nov. 2014.
[49] S. Taller et al., "Multiple ion beam irradiation for the study of radiation damage in materials," *Nucl. Instrum. Methods Phys. Res. B, Beam Interact. Mater. At.*, vol. 412, pp. 1–10, Dec. 2017.
[50] C. J. Capon, M. Brown, and R. R. Boyce, "Scaling of plasma-body interactions in low Earth orbit," *Phys. Plasmas*, vol. 24, no. 4, Apr. 2017, Art. no. 042901, doi: 10.1063/1.4979191.
[51] F. B. Leahy, "Cross-program design specification for natural environments (DSNE)," Nat. Aeronaut. Space Admin., Washington, DC, USA, Tech. Rep. SLS-SPEC-159, 2021.
[52] P. Li, N. Hershkowitz, and G. Severn, "Building Langmuir probes and emissive probes for plasma potential measurements in low pressure, low temperature plasmas," *J. Visualized Experiments*, vol. 171, p. 61804, May 2021.
[53] F. F. Chen, "Langmuir probe diagnostics," in *Proc. IEEE-ICOPS Meeting*, Jeju, South Korea, Jan. 2003, vol. 2, no. 6, pp. 1–42.
[54] R. B. Lobbia and B. E. Beal, "Recommended practice for use of Langmuir probes in electric propulsion testing," *J. Propuls. Power*, vol. 33, no. 3, pp. 566–581, May 2017.
[55] K. Wilson, Á. Romero-Calvo, M. Bengtson, J. Hammerl, J. Maxwell, and H. Schaub, "Development and characterization of the ECLIPS space environments simulation facility," *Acta Astronautica*, vol. 194, pp. 48–58, May 2022.
[56] D. A. Dahl, "SIMION for the personal computer in reflection," *Int. J. Mass Spectrometry*, vol. 200, nos. 1–3, pp. 3–25, Dec. 2000. [Online]. Available: https://www.sciencedirect.com/science/article/pii/S1387380600003055
[57] K. Champion and H. Schaub, "Ion optics for laboratory spacecraft wake generation," in *Proc. Spacecraft Charging Technol. Conf.*, Avignon, France, Jun. 2024, pp. 1–9.

Kaylee Champion received the B.S. degree in aerospace engineering from The University of Texas at Austin, Austin, TX, USA, in 2021, and the M.S. degree in aerospace engineering sciences from the University of Colorado at Boulder, Boulder, CO, USA, in 2023.

She is currently a Graduate Research Assistant and an NSTGRO Fellow with the University of Colorado at Boulder. She was with the Air Force Research Laboratory, NASA Goddard Space Flight Center, Greenbelt, MD, USA; NASA Marshall Space Flight Center, Huntsville, AL, USA; and the Jet Propulsion Laboratory, Pasadena, CA, USA. Her research interests include spacecraft-plasma interactions, charged astrodynamics, and vacuum chamber experimentation.

Ms. Champion is an NSF Fellow in 2021 and Zonta International Amelia Earhart Fellow in 2022.

Hanspeter Schaub is currently a Distinguished Professor and the Chair of the Department of Aerospace Engineering Sciences, University of Colorado at Boulder, Boulder, CO, USA. He holds the Schaden Leadership Chair. He has over 30 years of research experience, of which four years are at Sandia National Laboratories, Albuquerque, NM, USA. This has led to about 228 journals and 371 conference publications, and a fourth edition textbook on analytical mechanics of space systems. His research interests are in astrodynamics, relative motion dynamics, charged spacecraft motion, and spacecraft autonomy.

Dr. Schaub is a fellow of AIAA and AAS and a member of the National Academy of Engineering in 2025. In 2023, he won the Hazel Barnes Prize, the top award granted to Faculty at the University of Colorado at Boulder. He was awarded the H. Joseph Smead Faculty Fellowship, the Provost's Faculty Achievement Award, the Faculty Assembly Award for excellence in teaching, and the Outstanding Faculty Advisor Award, and has won the AIAA/ASEE Atwood Educator Award, AIAA Mechanics and Control of Flight Award, and the Collegiate Educator of the Year for the AIAA Rocky Mountain Section. He was the ADCS lead in the CICERO mission, the ADCS algorithm lead on a Mars mission, and supporting ADCS for a new asteroid mission.